Acta Crystallographica Section A
Foundations of Crystallography
ISSN 0108-7673

Received 1 October 2007
Accepted 3 December 2007

The MEM/Rietveld method with nano-applications – accurate charge-density studies of nano-structured materials by synchrotron-radiation powder diffraction

Masaki Takata

RIKEN/SPring-8 and CREST/JST, 1-1-1 Kouto, Hyogo, 679-5148, Japan, JASRI/SPring-8, 1-1-1 Kouto, Hyogo, 679-5198, Japan, and Department of Advanced Materials Science, School of Frontier Science, The University of Tokyo, Tokyo, Japan. Correspondence e-mail: takatama@spring8.or.jp

Structural studies of materials with nano-sized spaces, called nano-structured materials, have been carried out by high-resolution powder diffraction. Our developed analytical method, which is the combination of the maximum-entropy method (MEM) and Rietveld refinement, the so-called MEM/Rietveld method, has been successfully applied to the analysis of synchrotron-radiation (SR) powder diffraction data measured at SPring-8, a third-generation SR light source. In this article, structural studies of nano-porous coordination polymers and endohedral metallofullerenes are presented with the advanced technique of SR powder experiment. The structure of the adsorbed guest molecule in the coordination polymer and encapsulated atoms in the fullerene cage are clearly revealed by the MEM charge density. The methodology of MEM/Rietveld analysis is also presented.

1. Introduction: MEM application to nano-materials crystallography

Nano-structured materials, materials with nano-space, have attracted wide interest in the field of nano-materials science due to the huge potential for discovering novel physical properties. During the past two decades, several intriguing physical properties, such as ferromagnetism of K-doped zeolites (Nozue *et al.*, 1992), superconductivities of Ba-doped clathrate (Kawaji *et al.*, 1995) and electride (Miyakawa *et al.*, 2007), and photodimerization in a coordination cage (Takaoka *et al.*, 2006), have been found in nano-structured materials by doping of atoms and molecules into their nano-space.

The accurate structures of the nano-structured materials including doped atoms/molecules are always required for understanding the origin of characteristic properties. However, it is normally difficult to reveal structural information of doped guest atoms and molecules due to disorder and/or movement of guests. In addition, newly synthesized nano-structured materials are usually obtained in powder form. Thus, it is important to develop the powder diffraction instruments and data-analysis techniques for the structural analysis of novel nano-structured materials.

Since 1995, we have developed an elaborate charge-density refinement method, MEM/Rietveld method, which is based on information theory, the maximum-entropy method (MEM) using synchrotron-radiation powder data. The application of the MEM to crystallography extended the limits of the crystal-structure-analysis technique (Collins, 1982; Wilkins *et al.*, 1983; Bricogne, 1988; Bricogne & Gilmore, 1990; Sakata & Sato, 1990; Bricogne, 1993; de Vries *et al.*, 1994; Sivia & David, 1994; Papoular & Cox, 1995; Gilmore, 1996; Takata & Sakata, 1996; Marks & Landree, 1998; Burger & Prandl, 1999; Graafsmaa & de Vries, 1999). The MEM can yield a high-resolution electron-density distribution from a limited number of diffraction data. This ability of the MEM can be interpreted as 'imaging of diffraction data' (Takata & Sakata, 1996) as if the MEM were the virtual imaging lens by means of a computer program as shown in Fig. 1. Consequently, the concept led to the

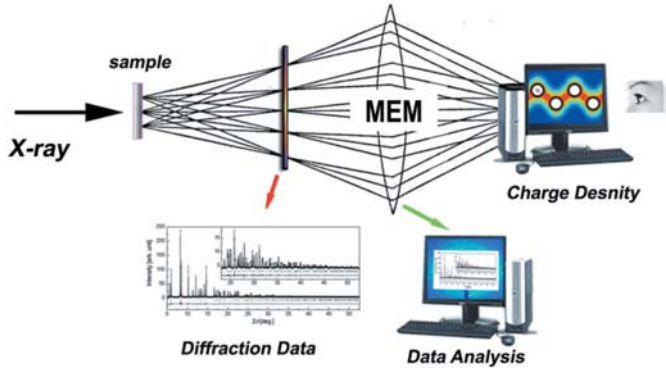

Figure 1
MEM virtual imaging lens by means of a computer program.

subsequent advancement of the MEM application, which is the development of the MEM/Rietveld method.

The first successful application of the MEM/Rietveld method was the determination of the endohedral nature of a metallofullerene, $Y@C_{82}$ (Takata *et al.*, 1995). The encapsulation of a Y atom in the nano-space of the fullerene cage was clearly visualized. The integration of the MEM charge-density imaging with Rietveld powder data fitting analysis (Rietveld, 1969) allowed us the systematic prediction of the Y-atom position and the rotational order of the fullerene cage in the iterative structure refinement. Since then, the method has been further applied to the structure determination of nano-structured materials such as a gas molecule adsorbed in a nano-porous coordination polymer (Kitaura *et al.*, 2002) and electrides (Kim *et al.*, 2007). The powder diffractometer installed at the SPring-8, BL02B2 beamline (Nishibori, Takata, Kato *et al.*, 2001; Takata *et al.*, 2002) has significantly contributed to the development and application of the MEM/Rietveld method. Characteristic structural features of other materials, orbital ordering (Takata, Nishibori, Kato *et al.*, 1999; Kato, Takata *et al.*, 2005; Kato, Ohishi *et al.*, 2005) and/or charge-transfer ordering (Aoyagi *et al.*, 2004; Kato *et al.*, 2003) as well as bonding nature (Nishibori, Takata, Sakata, Tanaka *et al.*, 2001) have also been successfully visualized by MEM/Rietveld analysis using a diffractometer. This review describes recent structural studies of nano-structured materials, coordination polymers and endohedral metallofullerenes by the MEM/Rietveld method using high-resolution powder data at SPring-8.

2. Synchrotron-radiation powder diffraction experiment

Following a great demand by materials scientists for synchrotron-radiation (SR) powder diffractometry, a large Debye–Scherrer camera was designed and installed at BL02B2 at SPring-8 (Nishibori, Takata, Kato *et al.*, 2001; Takata *et al.*, 2002). The schematic representation of the large Debye–Scherrer camera is shown in Fig. 2. To take advantage of the high-brilliance and high-energy beam, the camera method with transmission geometry was adopted. The 2θ dependence of the absorption effect by the specimen can be minimized even for materials containing heavy elements by selecting the proper X-ray energy and capillary diameter. The camera is equipped with a curved Imaging-Plate (IP) detector. The radius of the camera is 286.48 mm which determines the resolution to be 0.01° in 2θ due to the 50 × 50 µm pixel size of the IP. The size of the IP detector is 200 mm in width and 400 mm in length, which covers up to 80.0° in 2θ. Taking into account the utilization of short-wavelength incident X-rays, that is to say 0.35–1.0 Å, the maximum angle can cover a much wider range of reciprocal space (d > 0.3–0.8 Å) than in the case of Cu $K\alpha$. It is possible to record multi-powder patterns (maximum 30) on one IP detector using a mask with a vertical slit attached before the IP detector as shown in Fig. 2. This is particularly convenient for the investigation of structural changes induced by temperature (Kato *et al.*, 2002), light (Kato *et al.*, 2007) and gas adsorption (Kitaura *et al.*, 2002). To change the temperature of powder specimens, three different devices are available depending on the temperature required. They are high-temperature (300–1000 K) and low-temperature (90–300 K) N_2 gas-flow apparatus, and the Displex-type He cryostat (15–300 K). For all the experiment modes, the sample capillary can be oscillated with an ω stage during measurement to reduce the intensity inhomogeneity of Debye–Scherrer rings caused by the coarse granularity effect of the powder specimen.

A simple gas-import system for *in situ* gas-adsorption experiments is also available for the large Debye–Scherrer camera as schematically shown in Fig. 2. The first *in situ* SR powder diffraction study was carried out for hydrothermal conversion of zeolites by Norby (1997) with a similar system.

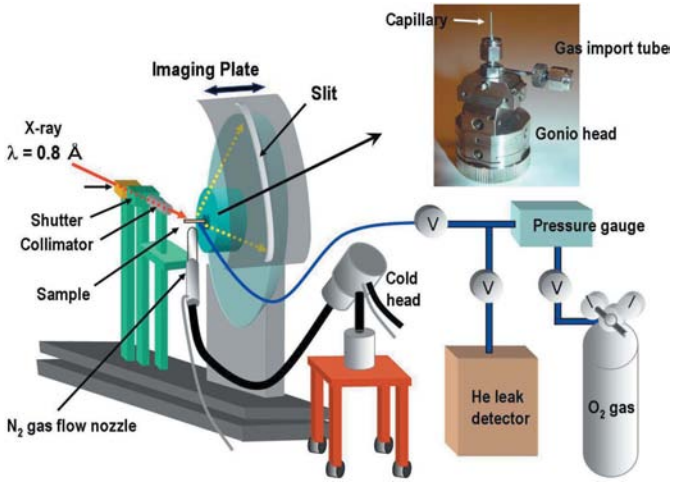

Figure 2
Schematic illustration of a large Debye–Scherrer camera and *in situ* gas adsorption experiment system at BL02B2 SPring-8. A photograph of the sample holder with a gas import tube is inserted.

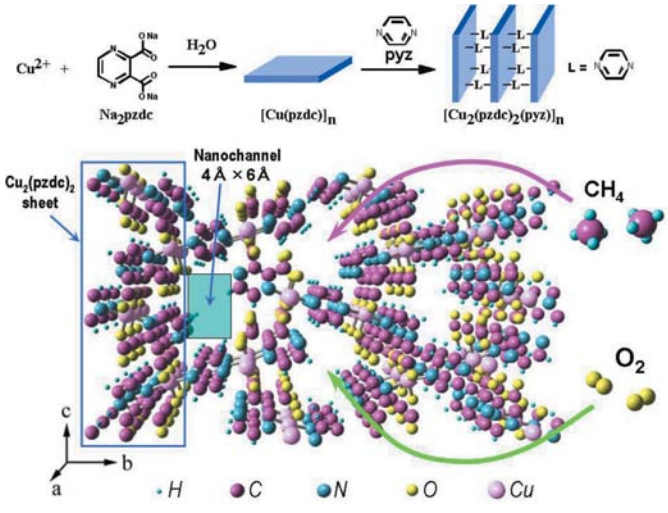

Figure 3
Crystal structure of CPL-1 and schematic procedure of synthesis of pillared-layer structure.

The capillary containing the powder specimen was attached to the stainless-steel tube using an epoxy adhesive. It was mounted in the special sample holder for the gas introduction, which was constructed from Swagelok parts and a steel tube. A stainless-steel tube attached to the sample holder was connected to the gas-handling system with a number of valves and a pressure gauge. A helium leak detector was connected to the system for leak checking of the evacuation and vacuum.

As a typical example of an *in situ* powder diffraction measurement of gas adsorption, the oxygen-adsorption investigation on a type of copper coordination polymer is described (Kitaura *et al.*, 2002). The sample used was $[Cu_2(pzdc)_2(pyz)]_n$ (pzdc: pyrazine-2,3-dicarboxylate, pyz: pyrazine) called CPL-1 (coordination polymer 1 with a pillared-layer structure) with uniform nanochannels of 4×6 Å (Kondo *et al.*, 1999). The crystal structure of CPL-1 is shown in Fig. 3. This material is well known to adsorb gas molecules inside the nanopores. However, there had been no structural evidence of the absorption site and the molecular structure inside the nanopores. Before the measurement of gas adsorption, the water molecules or organic solvent inside the nanopores must be removed. Using this system, the sample is easily degassed by heating the sample during evacuation. The sample of CPL-1 was degassed for approximately 10 min at 373 K to remove water molecules inside the nanopores. The oxygen was then introduced at 80 kPa at room temperature. The gas adsorption state was controlled by the temperature of the sample under a constant gas pressure. Because a powder sample is small, *i.e.* less than a few milligrams, the temperature is easier to control than the gas pressure. The temperature of the sample was gradually lowered from 300 to 90 K to initiate the gas adsorption. The measured powder diffraction patterns of CPL-1 with the adsorption of oxygen are shown in Fig. 4. Dramatic changes of the peak positions and relative intensities of reflections were observed between 150 and 130 K. These changes are thought to be caused by the adsorption of oxygen. To obtain data with much higher counting statistics for precise charge-density analysis, the exposure time is determined from the maximum limit of counting by an IP. In the present case, the data for charge-density analysis were measured with an exposure time of 65 min. After this measurement, the sample was heated to 300 K and the diffraction pattern changed to that of anhydrous CPL-1. The desorption of oxygen and the recovery of the empty structure without a collapse of the framework were confirmed.

3. Structural analysis by the MEM/Rietveld method

In 1995, the MEM/Rietveld method (Takata *et al.*, 1995) was developed for precise structure analysis using X-ray powder diffraction data. The method enables us to construct the fine structural model up to the charge-density level. This provides an efficient way for structure analysis with a self-consistent structure modeling by MEM charge-density imaging and Rietveld powder-pattern fitting based on the model derived from MEM charge density. At the start of the iteration, it is necessary to have a primitive structural model. The Rietveld method using this primitive structural model is called the pre-Rietveld analysis. It is well known that the MEM can provide useful information purely from observed structure-factor data beyond a presumed crystal structure model used in the pre-Rietveld analysis. This visualization ability of high-resolution

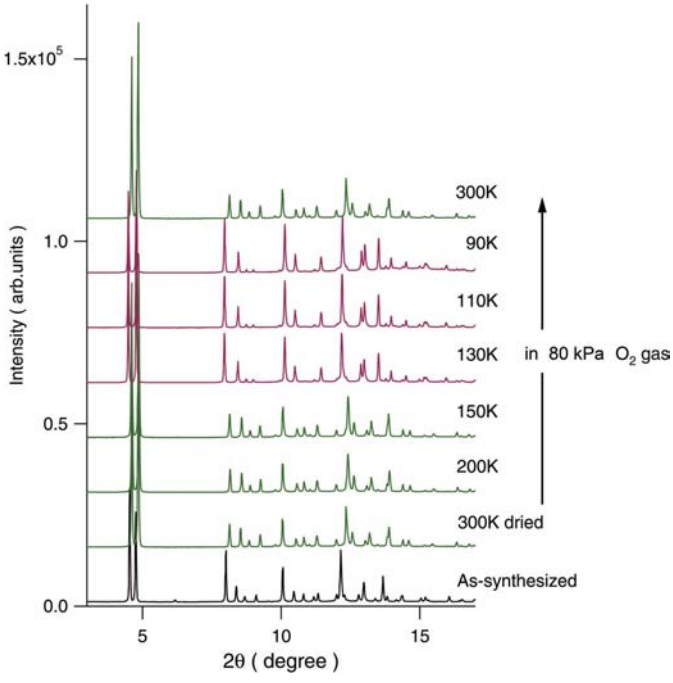

Figure 4
In situ SR powder diffraction patterns of CPL-1 with the adsorption of oxygen at 80 kPa. The diffraction pattern of as-synthesized CPL-1 is also shown. The wavelength of the incident X-rays is 0.8 Å.

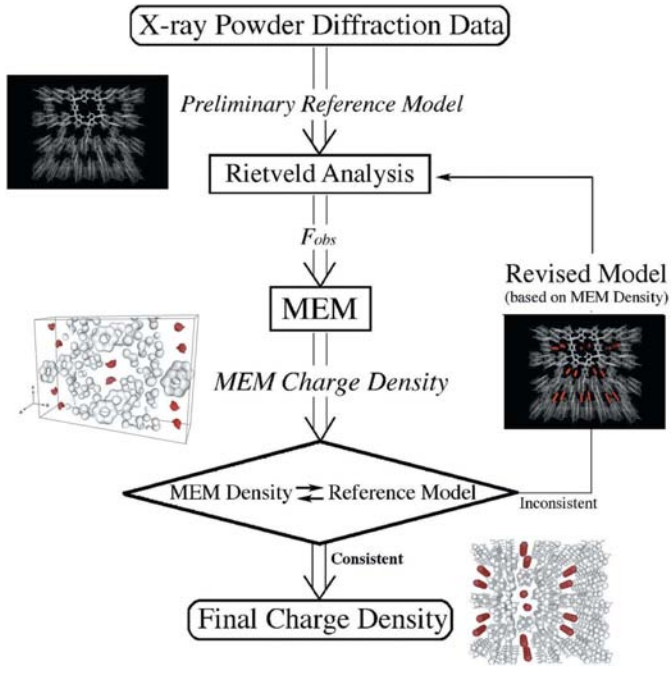

Figure 5
Flow chart of the MEM/Rietveld method with structure modeling and imaging of charge density.

charge density was useful to construct structure models of novel nano-structured materials.

The flow chart of the method is shown in Fig. 5 with an example of the structure-analysis procedure for a porous coordination polymer CPL-1 with the adsorption of O_2. In the first step of the analysis, the Rietveld refinement was carried out *via* a primitive structural model of only the CPL-1 framework determined by single-crystal X-ray diffraction (Kondo *et al.*, 1999), without assuming any guest molecules inside the nanopores. In the refinement, a rigid-body model and restraints for intermolecular distances and the angles were appropriately applied so as to maintain intrinsic molecular forms. The result of this Rietveld fitting is shown in Fig. 6(*a*). The misfitting of the observed and calculated powder patterns was largely due to the lack of guest gas molecules in the primitive structural model. Reliability factors based on the whole powder profile, R_{WP}, and the Bragg integrated intensities, R_I, were 16.4 and 44.9%, respectively. Despite the unsatisfactory fit to the data, the integrated intensities of each reflection were evaluated from the observed diffraction patterns using the result of the Rietveld refinement. Actually, the diffraction intensity of each data point is partitioned between each contributing reflection using the proportion of the calculated intensities in accordance with the following equation:

$$Y_i^{\rm obs}(2\theta_j) = Y^{\rm obs}(2\theta_j)\frac{Y_i^{\rm calc}}{\sum_i^n Y_i^{\rm calc}(2\theta_j)}, \qquad (1)$$

where $Y^{\rm obs}(2\theta_j)$ is the observed diffraction intensity at $2\theta_j$ and has contributions from N reflections, $Y_i^{\rm calc}(2\theta_j)$ is the calculated intensity from the structural model in the Rietveld analysis for the ith reflection at $2\theta_j$ and $Y_i^{\rm obs}(2\theta_j)$ is the contribution from the ith reflection at $2\theta_j$. This operation is carried out for all data points as shown in Fig. 7. As a result, all of the observed intensities were divided into each reflection without exception, and the integrated intensities of each reflection based on the observed data were estimated. The structure factors derived from these integrated intensities were used in the MEM analysis with the phases calculated from the structural model.

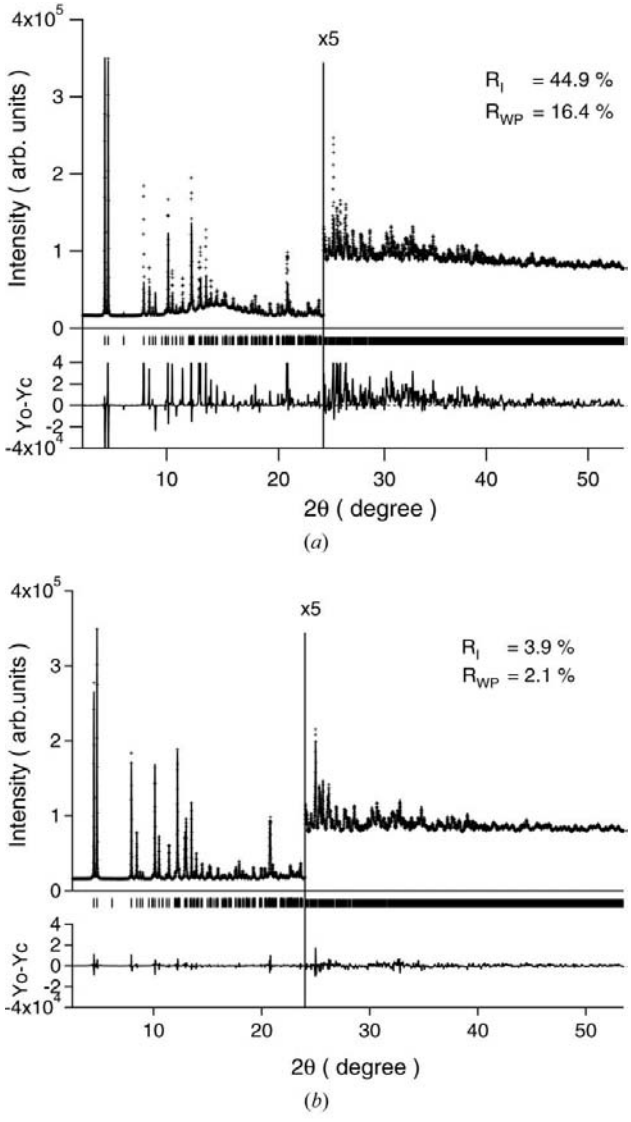

Figure 6
Fitting results of Rietveld refinement for CPL-1 with the adsorption of oxygen. (*a*) Initial refinement using a structural model of CPL-1 framework without guest molecules. (*b*) Final refinement using the modified structural model of CPL-1 with oxygen.

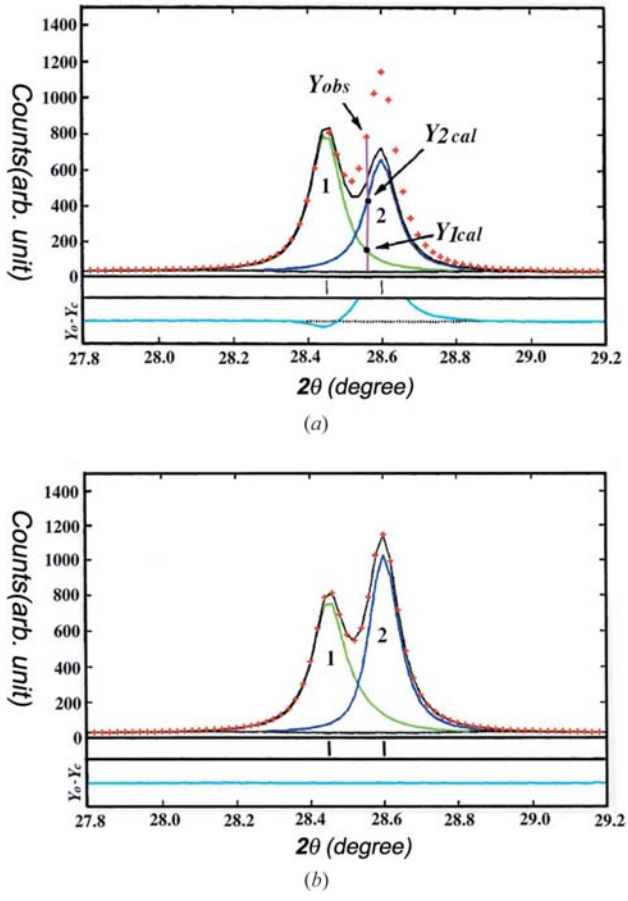

Figure 7
The procedure of evaluation of observed integrated intensities in MEM/Rietveld analysis. Difference plot (*a*) for the result of Rietveld refinement and (*b*) based on the evaluated intensities.

MEM calculation was carried out using a computer program, *ENIGMA* (Tanaka *et al.*, 2002). In the MEM calculation, the total number of electrons in the unit cell was given as a constraint. The number of electrons for adsorbed gas molecules was included in this calculation. The number of adsorbed gas molecules was independently examined by the gas adsorption isotherm. The obtained three-dimensional MEM charge-density distribution is shown at the middle left in Fig. 5. The framework structure can be clearly seen. Despite the use of a structural model without assuming guest molecules, two local peaks of charge density were recognized in each pore. It means that the diffraction intensities firmly contain the information of the adsorbed O_2 molecule.

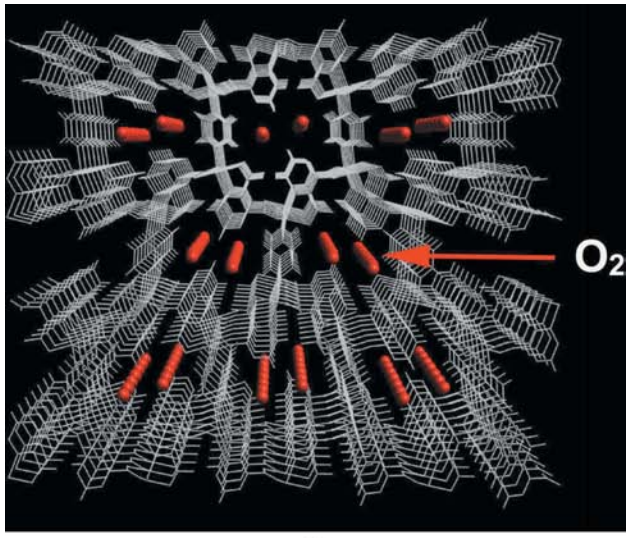

(*a*)

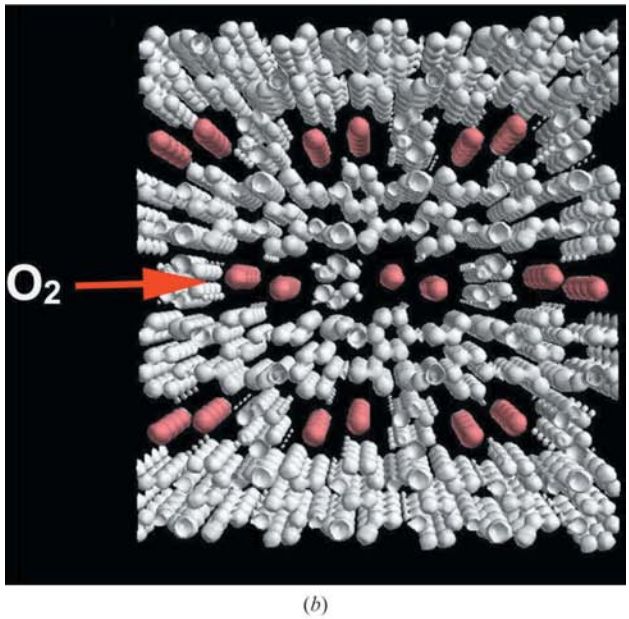

(*b*)

Figure 8
(*a*) Crystal structure of CPL-1 with the adsorption of O_2. O_2 molecules are shown by red balls. Other atoms are shown by connecting lines. (*b*) MEM charge density of CPL-1 with the adsorption of O_2 as an equi-density contour surface. The equi-density level is 1.0 e Å^{-3}. O_2 molecules are indicated in red.

As the next step in the analysis, the modified structural model including O_2 molecules based on the local peak positions in the nanochannel was applied as a new model to the second Rietveld refinement. The results of the final Rietveld refinement are shown in Fig. 6(*b*), which indicates a satisfactory fitting as a published structure determination. Reliability factors R_{WP} and R_I were dramatically improved to 2.1 and 3.9%, respectively. The feature of the obtained MEM charge density was consistent with the structural model used in Rietveld refinement at the atomic level and thus it was judged to be the final result of this analysis. The determined MEM charge density is shown in Fig. 8 with the structural model. The details of the charge density will be explained in the next section.

As shown here, the MEM/Rietveld method, which has the combined abilities of the structural model prediction of the MEM and the powder-pattern decomposition of the Rietveld method, was proved to be useful for the structure determination of porous coordination polymers undergoing gas adsorption. This method is also powerful for the structure determination of the rotational or positional disorder of molecules and organic ligands as well as metals and molecules in the fullerene cage for which their structural model is difficult to express and build.

4. Gas molecule in nanopores of a coordination polymer

Porous coordination polymers (Yaghi *et al.*, 2003; Kitagawa *et al.*, 2004) have attracted the attention of scientists for a number of reasons including the creation of nano-sized spaces and discovering novel phenomena as well as commercial interests such as their application in gas separation (Matsuda *et al.*, 2005), gas storage (Noro *et al.*, 2000; Férey *et al.*, 2003; Rowsell *et al.*, 2004) and heterogeneous catalysis (Seo *et al.*, 2000; Ohmori & Fujita, 2004). To develop novel porous coordination polymers as functional materials, the precise structural information of guest molecules and host framework are indispensable. We have successfully revealed specific molecular arrangements in the nanopores and molecular interactions between the guest molecules and host framework by the MEM/Rietveld method and *in situ* SR powder diffraction experiments of gas adsorption.

4.1. One-dimensional array of the O_2 molecule

As shown in Fig. 8, we have succeeded in direct observation of the O_2 molecule adsorbed in CPL-1 (Kitaura *et al.*, 2002). The result gave a conclusive answer to the long-standing question of where the gas molecules locate inside the nanopore. In Fig. 8, the dumbbell-shaped electron densities, which are presumably due to O_2 molecules, are clearly recognized in the middle of the nanochannels. There are 15.8 (1) electrons in total around the electron distribution, calculated on the basis of the MEM charge density, which virtually agrees with the number in the O_2 molecule. Therefore, we deduced that the dumbbell-shaped electron densities are O_2 molecules and one

O_2 molecule was adsorbed per Cu atom without any charge transfer between O_2 molecules and/or O_2 molecules and pore wall. No electron density showing chemical bonding is seen between the O_2 molecule and the pore walls. The interatomic distances between the O_2 molecule and the atoms on the pore walls are from approximately 2.7 to 3.3 Å, which shows the van der Waals contact of these atoms. These observations support the idea that O_2 molecules are physisorbed in the nanochannels of CPL-1. The isotropic temperature factor B of the O_2 molecule was refined to be 4.1 $Å^2$. This large value shows that the O_2 molecules have large thermal vibrations in the nanochannels. However, a clear charge-density distribution of adsorbed O_2 molecules shows that the molecules are strongly trapped at this position. The state of the oxygen in the nanochannels is thought to be closer to a solid state than a liquid state. As shown here, the distribution of the MEM charge density provides information on the molecular interaction, *i.e.* ionicity of atoms and the charge transfer between the molecules, because it is calculated for all of the electrons in the system.

The *in situ* SR powder experiment and the MEM/Rietveld analysis revealed that the restricted geometry achieved by one-dimensional nanochannels of CPL-1 leads to a specific molecular assembly, a one-dimensional ladder structure constructed by O_2 dimers, which is unlikely to be bulk fluid. This result will open up a new dimension of research on confined and ordered molecules within a restricted geometry. The O_2 molecule is well known to have paramagnetic property. The low-dimensional arrangement of molecular oxygen makes the investigation of the intermolecular potential and the quantum effect on magnetic properties attractive. Gas adsorption in the nanopores of a porous coordination polymer is a promising method by which to realize such an arrangement of molecular oxygen.

Fig. 9 shows the arrangement of the O_2 molecules in the nanochannel of CPL-1. Adsorbed O_2 molecules form a ladder structure. The intermolecular distance between the O_2–O_2 dimers is 3.28 Å, which is close to that in the α and β phases of solid O_2. On the other hand, the interdimer distance of 4.69 Å is relatively large. Theoretical studies have shown that the magnetic interaction between O_2 molecules depends strongly on the intermolecular distance and the orientation of the molecular axis (Bussery *et al.*, 1994). These results indicate that the interdimer interaction is approximately a hundred times weaker than the intradimer interaction. Therefore, the magnetic properties of this system are assumed to be equivalent to those for a Heisenberg antiferromagnetic dimer with $S = 1$. The temperature dependence of susceptibility and the high-field magnetization process at low temperatures were also investigated in terms of the magnetic property emanating from the one-dimensional order of the molecular O_2 arrangement in the nanochannel. Consequently, we found that an additional antiferromagnetic nature was caused by the ordered O_2 molecular array.

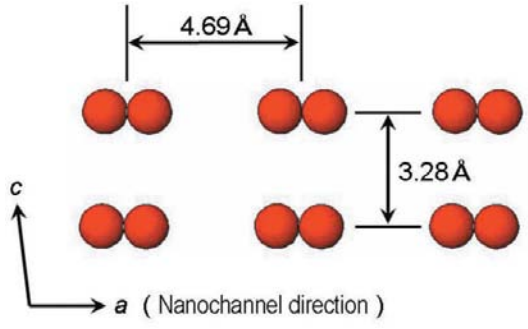

Figure 9
Arrangement of O_2 molecules in the nanochannel of CPL-1 viewed from the side of the nanochannel direction.

This work was the breakthrough,which gives a new concept of the novel functional material design by controlling molecular alignment using ordered nanopore structure of coordination polymers and leads to studies on various gas adsorption to porous coordination polymers such as H_2 (Kubota *et al.*, 2005), N_2, Ar, CH_4 (Kitaura *et al.*, 2005) and C_2H_2 (Matsuda *et al.*, 2005).

4.2. H_2 molecules align in nanochannels of CPL-1

It is a common assumption that the weak X-ray scattering amplitude of hydrogen makes it difficult to determine the H-atom position by X-ray structure analysis. However, the MEM/Rietveld analysis combined with high-brilliance SR

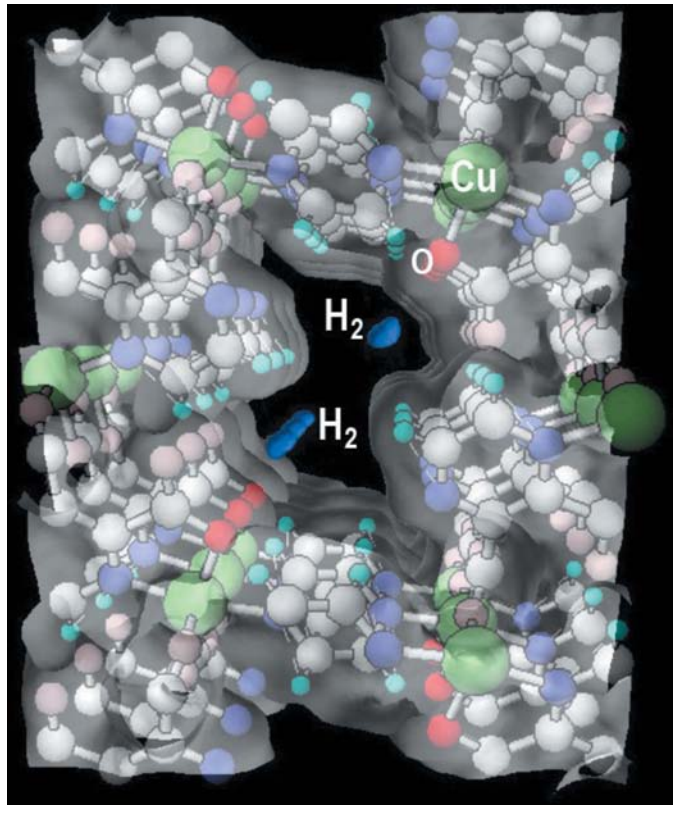

Figure 10
Close-up view of MEM charge-density distribution around an adsorbed H_2 molecule as an equi-density contour surface. The equi-density level is 0.11 e $Å^{-3}$. The structural model of the CPL framework is superimposed on the charge-density map.

powder diffraction enables us to reveal the position of H atoms as well as their chemical bonding (Noritake *et al.*, 2002; Kubota *et al.*, 2005). Adsorption of H_2 molecules in porous coordination polymers (Férey *et al.*, 2003; Rowsell *et al.*, 2004; Dybtsev *et al.*, 2004) is one of the most promising candidates. To develop the rational synthetic strategy for a novel porous coordination polymer for high-performance hydrogen storage, the elucidation of the intermolecular interaction between H_2 molecules and pore walls is essential. Thus, Kubota *et al.* carried out the structure determination of adsorbed hydrogen in the nanochannel of CPL-1 by SR powder diffraction and revealed that the H_2 molecules also produce a one-dimensional array in the nanochannel analogous to the case of the O_2 molecule (Kubota *et al.*, 2005).

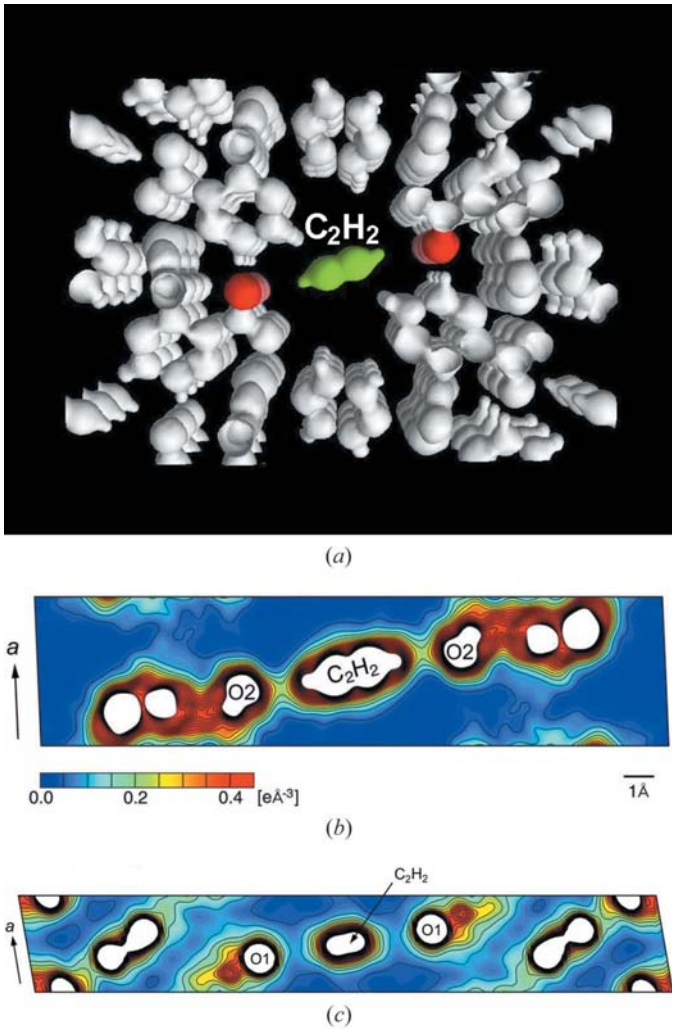

Figure 11
MEM charge-density distribution of CPL-1 with the adsorption of acetylene. (*a*) Three-dimensional MEM map as an equal-density contour surface viewed from the nanochannel direction. The equi-density level is 1.0 e Å^{-3}. The central C_2H_2 molecule and O atoms are represented by green and red, respectively. Section MEM charge densities containing the molecular axis of C_2H_2 and the *a* axis of (*b*) fully adsorbed phase and (*c*) intermediate adsorbed phase. Contour lines are drawn from 0.00 to 1.00 e Å^{-3} with intervals of 0.05 e Å^{-3}. Higher-density regions are omitted in the figure.

Distributions of the MEM charge density of CPL-1 with H_2 molecules are shown in Fig. 10. The small peak maxima of elongated-shape electron distribution of the H_2 molecule were observed inside the nanochannels. The position of the H_2 molecule is close to that of the O atom which belongs to the carboxylate group. The H_2 molecule seems to be locked in the concave space formed by the O atom and the H atom of pyrazine of the CPL framework. Interatomic distances between the H atoms of the H_2 molecule and the nearest O atom are 2.7 (1) and 2.4 (1) Å, respectively. They are comparable with the distances calculated from the van der Waals radii. The O atom to which the H_2 molecule is close forms a coordination bond with the Cu atom and is slightly negatively charged. The Cu–OOC moiety is thought to be associated with the attractive hydrogen accommodation. It is interesting that Rosi *et al.* (2003) showed a similar result in a metal–organic framework material different from CPL-1. They claim that the site around Zn and O is one of the H_2-molecule binding sites, found by inelastic neutron scattering spectroscopy. This suggests that the metal and oxygen bonded to it may play an important role in hydrogen adsorption. Moreover, the pocket of the cavity formed by the carboxylate group and the pyrazine is suited to the size of adsorbed H_2 molecules. Both the suitability of the pocket to the size of adsorbed molecules and the Cu–OOC moieties are considered to be closely related to the H_2-molecule adsorption in this system. Consequently, the first direct observation of the H_2 molecules adsorbed in the nanochannels of CPL-1 gives us promising guidelines in hydrogen-gas storage-material design.

4.3. Chemical adsorption of acetylene

The features of acetylene (C_2H_2) adsorption were quite different from that of other gases (Matsuda *et al.*, 2005). Fig. 11(*a*) shows the MEM charge density of a C_2H_2 molecule in CPL-1. The absorbed C_2H_2 molecule was clearly revealed as dumbbell-shaped electron densities with nipple-like projections. This interlayer dumbbell-shaped electron density of C_2H_2 molecules shows that one C_2H_2 molecule was adsorbed per two Cu atoms, which is different from the case of single molecules, O_2, N_2 and H_2, with one per Cu atom. Interestingly, C_2H_2 molecules align along the *a* axis with an inclination of 75.6° with an intermolecular distance of 4.78 Å. This long intermolecular distance means that C_2H_2 molecules are completely isolated from each other in the nanochannel of CPL-1. The section of electron density containing the molecular axis of C_2H_2 in Fig. 11(*b*) reveals that there exist a few electrons between the H atom of C_2H_2 and the O atom of the carboxylate in the host framework. This indicates that O···H—C hydrogen bonding, which includes not only electrostatic interactions between positively charged H atoms and negatively charged O atoms but also some covalent-bond-like interaction, plays an important role in the stabilization of C_2H_2 in the nanochannel. It is the nano-sized specific space provided by CPL-1 that realizes the unusual stable molecular array of C_2H_2, which is unlikely to correspond to bulk fluid. This specific C_2H_2 array including hydrogen-bonding

interactions was successfully characterized by the MEM/Rietveld method and SR powder diffraction.

The flexible framework arising from coordination bonds and the degrees of freedom of organic molecules is one of the most interesting characteristic features of coordination polymers (Matsuda *et al.*, 2004; Dybtsev *et al.*, 2004). The in-depth understanding of the intermediate adsorption state provides us with a feasible design for a porous framework, which changes their structure into that well suited for desired guest molecules and results in an efficient accommodation system. The structure of the intermediate adsorption state was further studied and determined as shown in Fig. 12 (Kubota *et al.*, 2006). The structural difference between fully and intermediate adsorption states was found to be the rotation of the C_2H_2 molecule in the nanochannel. The deformation of the CPL-1 framework structure was also found in association with molecular rotation. The obtained MEM charge density shows the clear disappearance of hydrogen bonding between the C_2H_2 molecule and pore wall indicating that the C_2H_2 molecules in the intermediate state are more freely located with weak bonding inside the nanochannel (Fig. 11*c*). The results suggested a scenario of C_2H_2 adsorption in CPL-1 in which C_2H_2 molecules are adsorbed freely in the early stage and form an intermediate state and ratchet to lock in the final stage.

Acetylene is one of the key molecules as a starting material for many chemical products and electric materials in the petrochemical and electronic industries. In order to obtain highly pure C_2H_2 for the preparation of these materials, the separation of C_2H_2 from the mixture gas containing CO_2 impurities without a large expenditure of energy is an important subject. In addition to this, acetylene is well known as a highly reactive molecule and, therefore, it cannot be compressed above 0.2 MPa; otherwise it explodes without oxygen, even at room temperature. Thus the result should open the door to create more feasible and safe materials for C_2H_2 separation.

Through this research we demonstrated that porous coordination polymers have a much more dynamic framework than is generally believed, and is characteristic of metal–organic species. The structural rearrangement of the host framework responding to guest molecules proceeds from the 'open' phase to the 'closed' phase. The structural findings by the MEM/Rietveld method would advance application of a unique class of materials, which cannot be obtained in rigid porous materials.

5. Metals in nano-space in a buckyball

Since the discovery of the buckyball molecule (Kroto *et al.*, 1985), fullerene, many studies have attempted to encapsulate metal atoms inside the 1 nm-scale space inside the buckyball to create novel functional nanomaterials. However, X-ray structure analysis had not been carried out in the first 5 years since the research started. The difficulties of X-ray structure analysis for metallofullerenes come from the fact that intrinsic orientational disorder of the fullerene cage and encapsulated metal atoms is rather common. In such a case, it may be

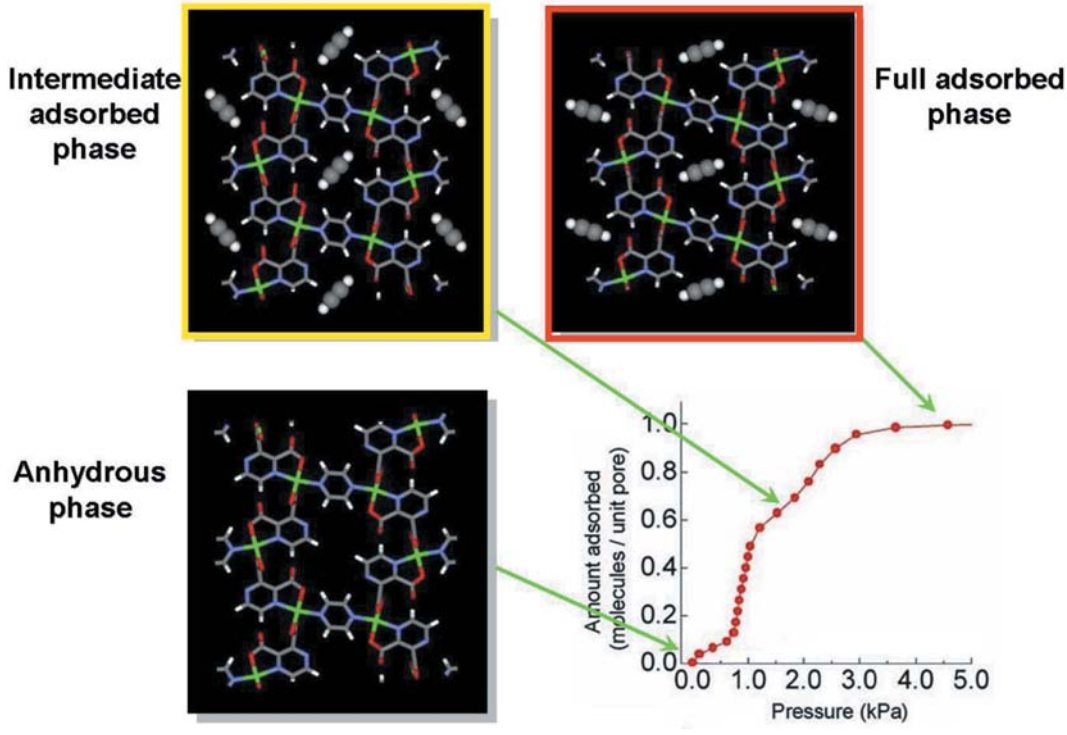

Figure 12
Acetylene adsorption isotherm and crystal structures of CPL-1 with adsorption of acetylene corresponding to the amount of adsorbed gas. These figures are viewed from the nanochannel direction. Acetylene molecules are shown by the space-filling model. Other molecules are shown by connecting lines.

extremely difficult to construct an adequate structural model. The MEM/Rietveld method succeeded in overcoming such difficulties by the ability of the MEM in terms of a model-free reconstruction of the charge densities from measured X-ray diffraction data when it is applied to accurate synchrotron powder data. Recently, details of characteristic features for atoms inside the buckyball such as multiple disorders of metal atoms and encapsulation of the C_2 molecule are clearly visualized from high-resolution powder data measured at SPring-8.

One of the most intriguing observations is a perfect pentagonal dodecahedron charge density formed by two La atoms in an icosahedron C_{80}-I_h cage (Nishibori, Takata, Sakata, Taninaka *et al.*, 2001). This novel shape of the charge density has been observed as a result of a highly selective trajectory of the two La atoms hopping along the hexagonal rings of the C_{80}-I_h polyhedral network. The three-dimensional equi-charge-density surface of charge density for the La atom in the $La_2@C_{80}$ molecule is shown in Fig. 13 with C_{80} model. Figs. 13(*a*) and (*b*) represent the top views along the S_{10} and C_2 axes of C_{80}-I_h, respectively. A pentagonal dodecahedron cage, which should be due to the charge density of the encaged La atoms, is clearly recognized inside the C_{80} cage. The theoretical study (Shimotani *et al.*, 2004) succeeded in the reproduction of this highly selective trajectory for the internal motion of the encaged La atoms by examination of the energetically stable position of the La atoms inside the C_{80} cage caused by charge transfer from fullerene cage to La atoms.

Recently similar pentagonal dodecahedron cages have also been found in C_{82}-based di-yttrium and di-scandium carbide endohedral metallofullerenes (Nishibori, Narioka *et al.*, 2006, Nishibori, Ishihara *et al.*, 2006). The MEM charge densities of encapsulated atoms Y_2C_2 for $(Y_2C_2)@C_{82}$(III) and Y_2 for $Y_2@C_{82}$(III) are shown in Figs. 14(*a*) and (*b*), respectively. Charge densities are inserted into the schematic structure of a C_{82}-C_{3V}(8) cage. The charge densities of two Y atoms for both Y_2C_2 and Y_2 are found to form pentagonal dodecahedra. In the case of $(Y_2C_2)@C_{82}$, the charge density colored blue is due to two C atoms encapsulated in the fullerene cage.

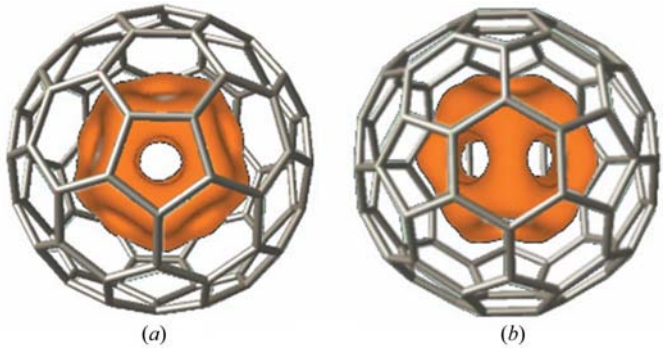

Figure 13
MEM charge densities of the encapsulated La2 pair as the equal density (1.7 e Å^{-3}) along the (*a*) S_{10} and (*b*) C_2 axes. The model of the C_{80}-I_h fullerene cage is represented by green sticks.

The pentagonal dodecahedral shape of charge densities due to Y_2 in both $(Y_2C_2)@C_{82}$(III) and $Y_2@C_{82}$(III) is identical to that observed for La_2 in $La_2@C_{80}$. The MEM charge density of La_2 in $La_2@C_{82}$ with schematic structure model of C_{80}-I_h is also shown in Fig. 14(*c*). In Fig. 14(*c*), the C atoms shared by three six-membered rings are shown as red balls, forming a pentagonal dodecahedron. The S_{10} axis is perpendicular to the figure plane. This orientation of the pentagonal dodecahedron is identical to that of Y_2C_2 (Fig. 14*a*) and Y_2 (Fig. 14*b*). In Figs. 14(*a*) and (*b*), the C atoms shared by three six-membered rings on the C_{82}-C_{3V}(8) cage are shown as blue balls. It is important to note that the arrangement of 16 out of 22 blue balls in Figs. 14(*a*) and (*b*) can be superimposed on red balls in Fig. 14(*c*) except for the topmost part. The superimposed part of the carbon cage of C_{82}-C_{3V}(8) and C_{80}-I_h is extracted and shown in Fig. 14(*d*). It is found that 16 out of 20 Y-atom peaks are located under the C atoms shared by three six-membered rings. In $La_2@C_{80}$, the pentagonal dodecahedral charge density is caused by a time-averaged feature of hopping La atoms as revealed by MEM charge density and theoretical studies. The two Y atoms in both $(Y_2C_2)@C_{82}$(III) and $Y_2@C_{82}$(III) are also hopping inside the C_{82}-C_{3V}(8) cage. An arrangement of the 20 Y_2 sites maintains the threefold symmetry which explains the previous ^{13}C NMR results (Inoue *et al.*, 2004).

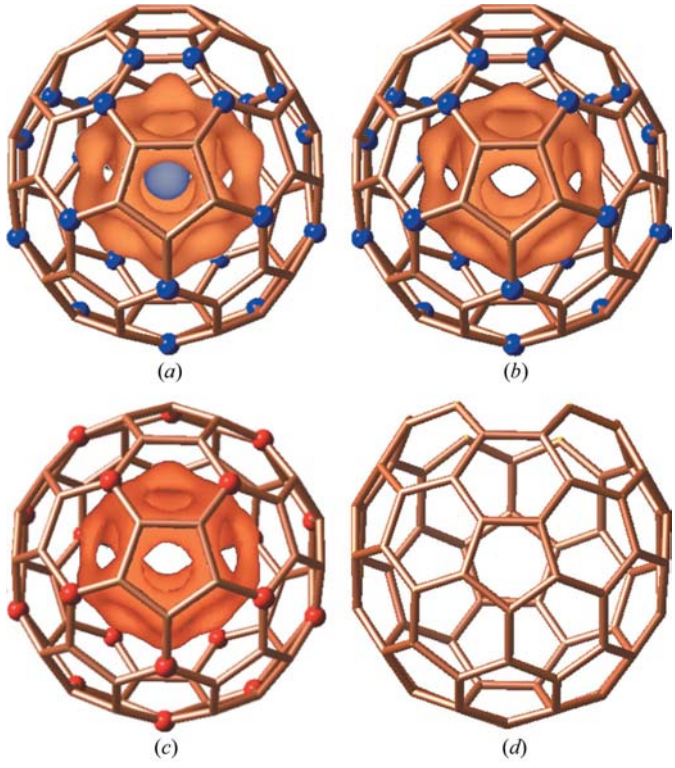

Figure 14
The equi-contour surface, 1.5 e Å^{-3}, of MEM charge density for (*a*) Y_2C_2, (*b*) Y_2 and (*c*) La_2. The charge densities are inserted into a schematic structure model of (*a*) and (*b*) C_{82}-C_{3V}(8) and (*c*) C_{80}-I_h fullerene cage. The Y and La charge densities are colored red. The C_2 charge densities are colored blue. (*d*) Schematic C-atom arrangement of the common part for C_{82}-C_{3V}(8) and C_{80}-I_h cages.

For two positively charged metal ions, the longer interatomic distance is favorable for reducing Coulomb repulsion. The formation of a pentagonal-dodecahedral charge density due to entrapped metal atoms is a rather common feature when two positively charged metal ions are trapped in a fullerene cage. In addition, encapsulated C_2 in $(Y_2C_2)@C_{82}$(III) are located at the center of the Y_2 pentagonal dodecahedron as if it is trapped in the Y_2 cage. The C_2 encapsulation to reduce the Coulomb repulsion between two negatively charged ions may frequently occur in other multi-metallofullerenes. The present results suggest the possibility of the existence of other carbon-encapsulated multi-metallofullerenes. Actually, the C_2 encapsulation of several multi-metallofullerenes such as Sc_3C_{82} and Sc_2C_{84} has been found after these studies.

6. Analysis resolution in the MEM/Rietveld method

It should be noted that the MEM/Rietveld method deduces the best possible averaged charge density of crystalline materials based simply on the *maxent* concept. Thus, the data reliability and resolution are strongly correlated to the result obtained. In the case of the endohedral metallofullerenes, critical examination had been required for the relationship between the observed data quality and the MEM charge density. The start of the discussion was the structure analysis of tri-Sc metallofullerene, Sc_3C_{82}. For the structure of Sc_3C_{82}, there had been two possibilities as $(Sc_3C_2)@C_{80}$ or $Sc_3@C_{82}$. Until then, we had reported a series of metal carbide (M_2C_2 species) encapsulated in a buckyball such as $(Sc_2C_2)@C_{84}$ (Wang *et al.*, 2001) and $(Y_2C_2)@C_{82}$(III) (Inoue *et al.*, 2004).

Our first report on the tri-Sc metallofullerene, Sc_3C_{82}, structure was the buckyball encapsulating an Sc_3 metal cluster. Sugai *et al.* (2001) have reported, however, the possibility of an endohedral metal carbide structure for $(Sc_3C_2)@C_{80}$ instead of $Sc_3@C_{82}$ by gas-phase ion mobility measurements. Actually, Iiduka *et al.* (2005) have recently shown that the fullerene cage of Sc_3C_{82} is C_{80}-I_h instead of C_{82} from ^{13}C NMR results on the $(Sc_3C_{82})^-$ anion, indicating the intact $(Sc_3C_2)@C_{80}$ carbide structure. Single-crystal X-ray structures of chemically functionalized $(Sc_3C_2)@C_{80}$ molecules with an addition of adamantylidene–carbine (Ad) have also been reported. However, X-ray structures of the intact $(Sc_3C_2)@C_{80}$ fullerenes had not been known until we reported them. Finally, Nishibori has realized that the best possible structure model building depends on the data resolution in the MEM/Rietveld analysis just as much as in the case with conventional structure analysis (Nishibori, Terauchi *et al.*, 2006). Here, the resolution effect in the MEM/Rietveld analysis of tri-scandium metallofullerene is described in some detail.

The key to the problem was a difference in quality of powder diffraction data measured at SPring-8 from that of the previous data (Takata, Nishibori, Sakata *et al.*, 1999). In our previous report, the data resolution of the second-generation SR data was $d > 2.1$ Å. In the analysis, the fullerene cage for Sc_3C_{82} was postulated as C_{82} (*i.e.* $Sc_3@C_{82}$) based on the mass spectral data and the disorder of the Sc atoms was not considered. These led us to erroneously assign $(Sc_3C_2)@C_{80}$ as $Sc_3@C_{82}$ in the analysis. SPring-8 has great advantages over previous sources to improve the quality of data due to the availability of high flux and high energy resolution X-ray photons. The maximum intensity of the Bragg reflections for the present data was around 1500000 counts, which is approximately four times larger than for the previous data. The widths of Bragg peaks for the present data were from 0.04 to 0.08° in 2θ. These are approximately 2/3 of that of the previous data. The larger intensities and higher angular resolution enable us to perform accurate and reliable MEM/Rietveld analyses because even the weak Bragg intensities become detectable. The data set with $d > 1.43$ Å d-spacing range was used in the present analysis.

In the present MEM/Rietveld analysis, a spherical shell composed of 82 C atoms and a toluene molecule was used for the first Rietveld refinement to avoid model-biased effects. The model bias may lead to a wrong structure. An X-ray diffraction experiment only measures the amplitude of the structure factors. The initial phases of the structure factors are estimated from a structural model adopted at the beginning of the analysis. The structure obtained by the analysis can be biased by the model adopted at the beginning. In this study, the least-biased structural model for the fullerene cage, which must be a spherical shell, was used as an initial model.

In total, 837 observed structure factors were extracted after the refinement. The MEM analysis was carried out by the program *ENIGMA* (Tanaka *et al.*, 2002). The MEM charge density at this stage is shown in Fig. 15(*a*). There are many peaks due to disorder of encapsulated Sc atoms in the MEM charge density of the fullerene cage. A relatively large peak seen at the center of the fullerene cage is assigned as C_2. The other peaks are assigned as disordered Sc atoms. Therefore, the fullerene cage is assigned as C_{80}.

In the previous MEM/Rietveld study on Sc_3C_{82}, only 279 structure factors were used in the MEM analysis because of the weak Bragg intensities around $d > 2.1$ Å d-spacing range. No charge density at the center of the fullerene cage was found in that analysis. The limited data resolution failed to reveal C_2 encapsulation. To confirm this point, the MEM analysis was preformed using only 279 reflections with $d >$ 2.1 Å d-spacing range with the SPring-8 data. The MEM charge density is shown in Fig. 15(*b*). The C_2 peak disappeared

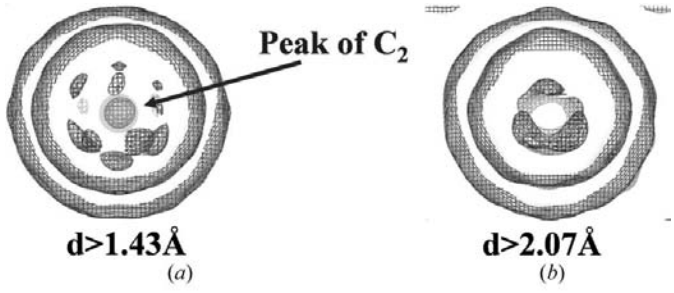

Figure 15
The equi-contour (0.7 e Å^{-3}) mesh of MEM charge densities for the $(Sc_3C_2)@C_{80}$ molecules based on a C_{82} spherical-shell model.

in the center of the fullerene cage, indicating that $d > 2.1$ Å resolution is not good enough to reveal a C_2 molecule in the C_{80} carbon cage. In the previous analysis, we assigned three Sc atoms to the three large electron-density peaks in Fig. 15(*b*). Then we investigated possible directions for two isomers of C_{82}-C_{3V} cages. The structure with the lowest reliability factors of Rietveld refinement was a final solution. The resulting fit of the Rietveld refinement using the previous $Sc_3@C_{82}$ model for present $d > 1.43$ Å data is shown in Fig. 16(*a*). In the $d > 2.6$ Å ($2\theta < 22^\circ$) range, the fit is satisfactory. However, in the $2.6 > d > 1.43$ Å range, there are large deviations indicating an incorrect structure. From these facts, it was concluded that the erroneous assignment of the previous analysis is mainly due to the lack of resolution in the analysis. The data accuracy and reliability in MEM electron-density analysis using powder data has also been discussed in the recent paper by Nishibori *et al.* (2007).

The result of the final Rietveld refinement for high-resolution $d > 1.43$ Å SPring-8 data is shown in Fig. 16(*b*). The reliability factors based on weighted profile, R_{wp}, and Bragg intensities, R_I, are as small as 2.60 and 4.36%, respectively. These values are lower than those of the previous study even in this high-resolution analysis. The lower reliability factors are satisfactory for the current precise structure determination.

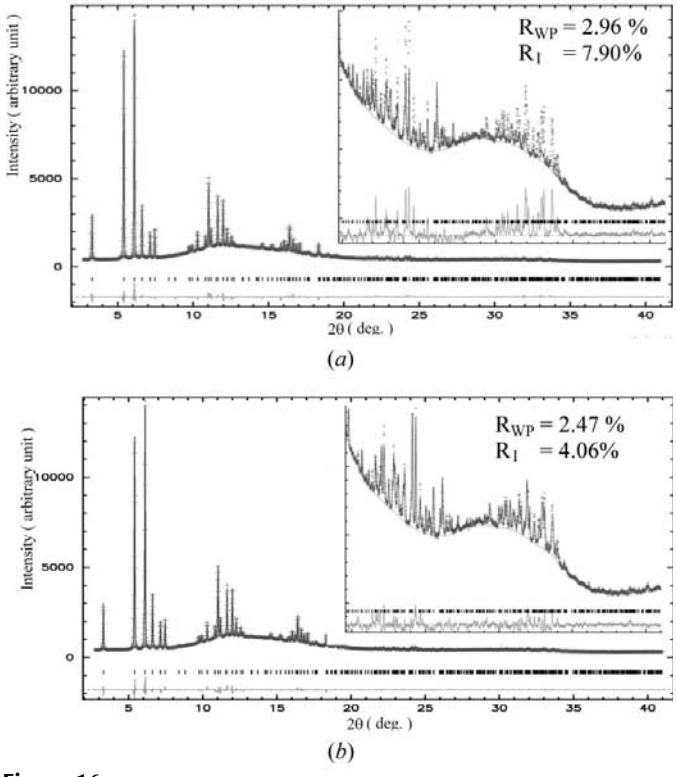

Figure 16
(*a*) The fitting results of Rietveld analysis using the $Sc_3@C_{82}$ structure model, which has been previously published (Takata, Nishibori, Sakata *et al.*, 1999). A close up of the region between 19.0 and 41.0° is shown in the inset. (*b*) The fitting result of the final Rietveld analysis for $(Sc_3C_2)@C_{80}$. A close up of the region between 19.0 and 41.0° is shown in the inset.

The molecular structure of the major part of $(Sc_3C_2)@C_{80}$ determined by the MEM/Rietveld method is shown in Figs. 17(*a*) and (*b*). The C_2 molecule is shown as one yellow sphere, since the MEM charge density for C_2 appears as one peak. In Fig. 17(*b*), the three Sc atoms and C_2 are located on the belt of the six-membered ring. The present structure is similar to the theoretically predicted structures by recent density functional theory (DFT) calculations (Tan & Lu, 2006). The deviations of the Sc–Sc and Sc–C distances between the present and the theoretical structures are within 0.15 Å.

It is noted that the erroneous assignment of the previous analysis is due to the lack of resolution of the powder data. The available data resolution of powder data is dramatically increased by the third-generation SR sources such as SPring-8. High-resolution data with the MEM/Rietveld method can determine the structures of endohedral metallofullerenes including disorder and/or motion of metal atoms such as the present $(Sc_3C_2)@C_{80}$ study.

7. Advanced application to structure–property relationship investigation

In this review, some recent structural studies of novel nanostructured materials, CPL-1 and endohedral metallofullerene by the MEM/Rietveld method using high-resolution powder data measured at SPring-8 are described. Accurate structural information, such as bonding nature, positions of H atoms and multiple disorder of metal atoms, have been clearly revealed from powder diffraction data alone. One of our main purposes in carrying out a MEM charge-density study is to investigate structure–property relationships in novel materials. Recent progress of MEM charge-density studies has been made in terms of the investigation of structure–electronic-property relationships.

As a recent application to the structure–conductivity relationship study of a nano-material, the structure determination of the nano-cage compound $12CaO \cdot 7Al_2O_3$ (C12A7) (Kim *et al.*, 2007) is presented. This material is synthesized from lime and alumina, both typical insulators. However, it was converted into an inorganic electride C12A7:e^- by the

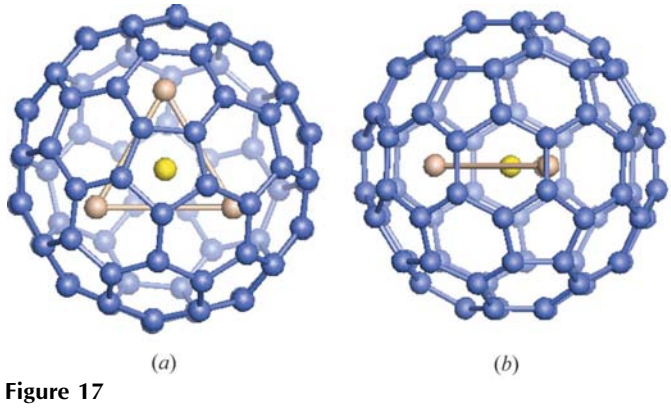

Figure 17
The molecular structure models of $(Sc_3C_2)@C_{80}$ along the (*a*) S_{10} and (*b*) C_2 axes determined by the MEM/Rietveld method from synchrotron X-ray powder diffraction data.

reduction of O^{2-} ions encapsulated in the nano-cage (Matsuishi *et al.*, 2003) (Fig. 18*a*). The electric and chemical properties of this material can be modified by the substitution of various encapsulated anions. In particular, the electrical transport nature from insulator to superconductor is recently reported (Miyakawa *et al.*, 2007). We succeeded in determining the complicated structure of C12A7 by MEM/Rietveld analysis (Fig. 18). As shown in Fig. 18(*b*), in insulating C12A7:O^{2-}, Ca atoms are displaced by the electrostatic interaction with a free O^{2-} ion in the cage and the cage is deformed. Free O^{2-} ions are randomly accommodated in two different cages out of twelve cages per unit cell to compensate for the charge of the framework. The splitting feature of the Ca-atom charge density indicates the mixture of regular cages and deformed cages. Consequently, the MEM charge density uncovered a new structural basis for the C12A7 conductivity (metal–insulator change), *i.e.* the cage structure homogeneity should be a key factor for the increase of the conductivity associated with substitution from O^{2-} ions to e^- doping (Fig. 18*c*).

Another remarkable example of methodological progress is the recent achievement of electrostatic potential and electric

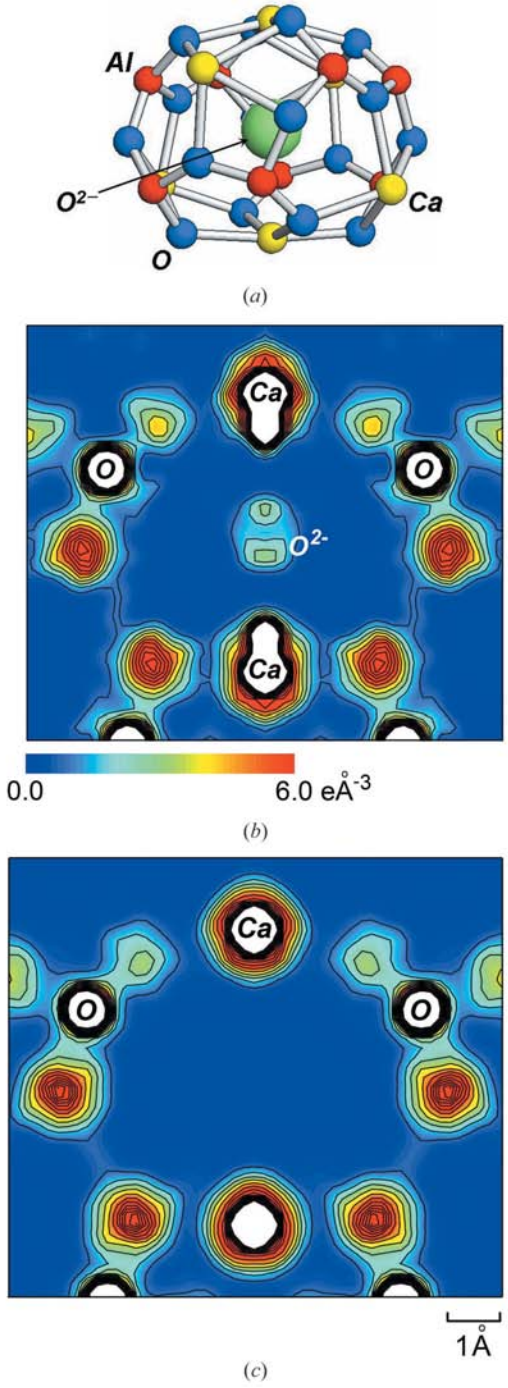

Figure 18
(*a*) Nano-cage structure of C12A7. MEM charge densities on the (001) plane for (*b*) C12A7:O^{2-} and (*c*) C12A7:e^- electride. Contour lines are drawn from 0.0 to 6.0 e Å^{-3} with intervals of 0.3 e Å^{-3}. Higher-density regions are omitted in the figure.

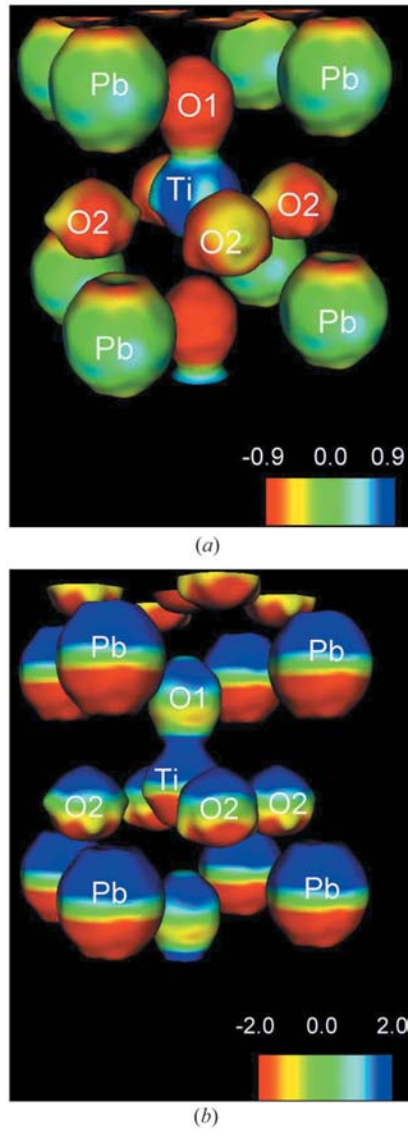

Figure 19
(*a*) Isosurface of charge density for $PbTiO_3$ at 0.86 e Å^{-3}. It is colored by the value of electrostatic potential from −0.9 (red) to 0.9 e Å (blue). (*b*) Isosurface of charge density for $PbTiO_3$ at 1 e Å^{-3}. It is colored by the amplitude of the z component of the electric field from −2.0 (red) to 2.0 e Å^{-2}.

field imaging based on MEM charge-density analysis (Tanaka *et al.*, 2006). As an example of the successful application of the method, the visualized electrostatic potential and electric field of the typical ferroelectric material, tetragonal $PbTiO_3$, are shown as iso-surfaces of charge density in Figs. 19(*a*) and (*b*), respectively. In Fig. 19(*a*), most of the iso-surface around the Pb ion is colored green. Note that the upper area of the surface is red, while the bottom area is yellow. This means that the center of electronic charge is shifted in the up–down direction relative to the center of the nucleus charge, which is evidence for the polarization of the Pb ion at the atomic level. Furthermore, the distribution of electric field shown in Fig. 19(*b*) agrees well with that obtained from the *ab initio* calculation (Cohen, 1992). These facts mean that our method is efficient for the experimental analysis of the electrostatic potential in crystalline materials. The application of the method is growing in the research area of nano-materials science such as gas absorbed in CPL-1. The experimental electrostatic potential would give crucial information, for example, to investigate interplay between the guest molecule and host framework.

Application of the MEM and the MEM/Rietveld method using SR data to nano-structured materials is coming into advanced use. For example, Sawa *et al.* (2005) have applied the MEM to the observation of a single H_2 molecule encapsulated in the fullerene cage of an aza-thia open-cage fullerene with SR single-crystal X-ray diffraction experiments. The clathrate-like cage structure by chemical bonding has been found in a binary $CoSb_3$ skutterudite (Ohno *et al.*, 2007), a promising thermoelectric material, by the MEM/Rietveld method using multi-SR powder data taken at SPring-8 (Nishibori *et al.*, 2007).

The method is now in a utilization phase as one of the proper techniques for thorough research into structure–property relationships of novel materials (for instance, Snyder *et al.*, 2004) and will extend the innovative contribution of crystallography in the materials science research area, *e.g.* by further application to topological analysis (Cargnoni *et al.*, 2004).

First, I would like to dedicate this article to Dr Makoto Sakata for his tutelage to me as a scientist and his excellent leadership on MEM charge-density research in crystallography. I thank Drs Yoshiki Kubota, Eiji Nishibori, Kenichi Kato and Hiroshi Tanaka for co-editing this article as the long-time primary key collaborators of MEM charge-density research. I also thank Dr Dave Cox for his helpful discussion in the early stage of development of the MEM/Rietveld method. The work on the endohedral metallofullerene is a collaboration with Dr Hisanori Shinohara and his collaborators. And the work on CPL-1 is a collaboration with Dr Susumu Kitagawa and his collaborators. The studies on C12A7 and $PbTiO_3$ are collaborations with Dr Hideo Hosono and Dr Yoshihiro Kuroiwa, respectively. This work was supported by the Grant-in-Aid for Scientific Research from the Ministry of Education, Science and Culture of Japan. The synchrotron-radiation X-ray powder diffraction experiments were performed at the SPring-8 BL02B2 beamline with approval of the Japan Synchrotron Radiation Research Institute (JASRI).

References

Aoyagi, S., Kato, K., Ota, A., Yamochi, H., Saito, G., Suematsu, H., Sakata, M. & Takata, M. (2004). *Angew. Chem. Int. Ed.* **43**, 3670–3673.
Bricogne, G. (1988). *Acta Cryst.* A**44**, 517–545.
Bricogne, G. (1993). *Acta Cryst.* D**49**, 37–60.
Bricogne, G. & Gilmore, C. J. (1990). *Acta Cryst.* A**46**, 284–297.
Burger, K. & Prandl, W. (1999). *Acta Cryst.* A**55**, 719–728.
Bussery, B., Umanskii, S. Y., Aubert-Frécon, M. & Bouty, O. (1994). *J. Chem. Phys.* **101**, 416–423.
Cargnoni, F., Nishibori, E., Rabiller, P., Bertini, L., Snyder, G. J., Christensen, M., Gatti, C. & Iversen, B. (2004). *Chem. Eur. J.* **10**, 3861–3870.
Cohen, R. E. (1992). *Nature (London)*, **358**, 136–138.
Collins, D. M. (1982). *Nature (London)*, **298**, 49–51.
Dybtsev, D. N., Chun, H. & Kim, K. (2004). *Angew. Chem. Int. Ed.* **43**, 5033–5036.
Férey, G., Latroche, M., Serre, C., Millange, F., Loiseau, T. & Percheron-Guégan, A. (2003). *Chem. Commun.* **24**, 2976–2977.
Gilmore, C. J. (1996). *Acta Cryst.* A**52**, 561–589.
Graafsma, H. & de Vries, R. Y. (1999). *J. Appl. Cryst.* **32**, 683–691.
Iiduka, Y., Wakahara, T., Nakahodo, T., Tsuchiya, T., Sakuraba, A., Maeda, Y., Akasaka, T., Yoza, K., Horn, E., Kato, T., Liu, M. T., Mizorogi, N., Kobayashi, K. & Nagase, S. (2005). *J. Am. Chem. Soc.* **127**, 12500–12501.
Inoue, T., Tomiyama, T., Sugai, T., Okazaki, T., Suematsu, T., Fujii, N., Utsumi, H., Nojima, K. & Shinohara, H. (2004). *J. Phys. Chem. B*, **108**, 7573–7579.
Kato, K., Moritomo, Y., Takata, M., Sakata, M., Umekawa, M., Hamada, N., Ohkoshi, S. & Tokoro, H. (2003). *Phys. Rev. Lett.* **91**, 255502.
Kato, K., Nishibori, E., Takata, M., Sakata, M., Nakano, T., Uchihira, K., Tsubota, M., Iga, F. & Takabatake, T. (2002). *J. Phys. Soc. Jpn*, **71**, 2082–2085.
Kato, K., Ohishi, Y., Takata, M., Nishibori, E., Sakata, M. & Moritomo, Y. (2005). *Phys. Rev. B*, **71**, 012404.
Kato, K., Takata, M., Moritomo, Y., Nakamoto, A. & Kojima, N. (2007). *Appl. Phys. Lett.* **90**, 201902.
Kato, K., Takata, M., Nishibori, E., Sakata, M., Hamada, N. & Moritomo, Y. (2005). *J. Phys. Soc. Jpn*, **74**, 2137–2140.
Kawaji, H., Horie, H., Yamanaka, S. & Ishikawa, M. (1995). *Phys. Rev. Lett.* **74**, 1427–1429.
Kim, S. W., Matsuishi, S., Nomura, T., Kubota, Y., Takata, M., Hayashi, K., Kamiya, T., Hirano, M. & Hosono, H. (2007). *Nano Lett.* **7**, 1138–1143.
Kitagawa, S., Kitaura, R. & Noro, S. (2004). *Angew. Chem. Int. Ed.* **43**, 2334–2375.
Kitaura, R., Kitagawa, S., Kubota, Y., Kobayashi, T. C., Kindo, K., Mita, Y., Matsuo, A., Kobayashi, M., Chang, H., Ozawa, T. C., Suzuki, M., Sakata, M. & Takata, M. (2002). *Science*, **298**, 2358–2361.
Kitaura, R., Matsuda, R., Kubota, Y., Kitagawa, S., Takata, M., Kobayashi, T. C. & Suzuki, M. (2005). *J. Phys. Chem. B*, **109**, 23378–23385.
Kondo, M., Okubo, T., Asami, A., Noro, S., Yoshitomi, T., Kitagawa, S., Ishii, T., Matsuzaka, H. & Seki, K. (1999). *Angew. Chem. Int. Ed.* **38**, 140–143.
Kroto, H. W., Heath, J. R., O'Brien, S. C., Curl, R. F. & Smalley, R. E. (1985). *Nature (London)*, **318**, 162–163.
Kubota, Y., Takata, M., Matsuda, R., Kitaura, R., Kitagawa, S., Kato, K., Sakata, M. & Kobayashi, T. C. (2005). *Angew. Chem. Int. Ed.* **44**, 920–923.

Kubota, Y., Takata, M., Matsuda, R., Kitaura, R., Kitagawa, S. & Kobayashi, T. C. (2006). *Angew. Chem. Int. Ed.* **45**, 4932–4936.
Marks, L. D. & Landree, E. (1998). *Acta Cryst.* A**54**, 296–305.
Matsuda, R., Kitaura, R., Kitagawa, S., Kubota, Y., Belosludov, R. V., Kobayashi, T. C., Sakamoto, H., Chiba, T., Takata, M., Kawazoe, Y. & Mita, Y. (2005). *Nature (London)*, **436**, 238–241.
Matsuda, R., Kitaura, R., Kitagawa, S., Kubota, Y., Kobayashi, T. C., Horike, S. & Takata, M. (2004). *J. Am. Chem. Soc.* **126**, 14063–14070.
Matsuishi, S., Toda, Y., Miyakawa, M., Hayashi, K., Kamiya, T., Hirano, M., Tanaka, I. & Hosono, H. (2003). *Science*, **301**, 626–629.
Miyakawa, M., Kim, S. W., Hirano, M., Kohama, Y., Kawaji, H., Atake, T., Ikegami, H., Kono, K. & Hosono, H. (2007). *J. Am. Chem. Soc.* **129**, 7270–7271.
Nishibori, E., Ishihara, M., Takata, M., Sakata, M., Ito, Y., Inoue, T. & Shinohara, H. (2006). *Chem. Phys. Lett.* **433**, 120–124.
Nishibori, E., Narioka, S., Takata, M., Sakata, M., Inoue, T. & Shinohara, H. (2006). *Chem. Phys. Chem.* **7**, 345–348.
Nishibori, E., Sunaoshi, E., Yoshida, A., Aoyagi, S., Kato, K., Takata, M. & Sakata, M. (2007). *Acta Cryst.* A**63**, 43–52.
Nishibori, E., Takata, M., Kato, K., Sakata, M., Kubota, Y., Aoyagi, S., Kuroiwa, Y., Yamakata, M. & Ikeda, N. (2001). *Nucl. Instrum. Methods Phys. Res. A*, **467–468**, 1045–1048,
Nishibori, E., Takata, M., Sakata, M., Tanaka, H., Muranaka, T. & Akimitsu, J. (2001). *J. Phys. Soc. Jpn Lett.* **70**, 2252–2254.
Nishibori, E., Takata, M., Sakata, M., Taninaka, A. & Shinohara, H. (2001). *Angew. Chem. Int. Ed.* **40**, 2998–2999.
Nishibori, E., Terauchi, I., Sakata, M., Takata, M., Ito, Y., Sugai, T. & Shinohara, H. (2006). *J. Phys. Chem. B*, **110**, 19215–19219.
Norby, P. (1997). *J. Am. Chem. Soc.* **119**, 5215–5221.
Noritake, T., Aoki, M., Towata, S., Seno, Y., Hirose, Y., Nishibori, E., Takata, M. & Sakata, M. (2002). *Appl. Phys. Lett.* **81**, 2008–2010.
Noro, S., Kitagawa, S., Kondo, M. & Seki, K. (2000). *Angew. Chem. Int. Ed.* **39**, 2082–2084.
Nozue, Y., Kodaira, T. & Goto, T. (1992). *Phys. Rev. Lett.* **68**, 3789–3792.
Ohmori, O. & Fujita, M. (2004). *Chem. Commun.* pp. 1586–1587.
Ohno, A., Sasaki, S., Nishibori, E., Aoyagi, S., Sakata, M. & Iversen, B. B. (2007). *Phys. Rev. B*, **76**, 064119.
Papoular, R. J. & Cox, D. (1995). *Europhys. Lett.* **32**, 337–342.
Rietveld, H. M. (1969). *J. Appl. Cryst.* **2**, 65–71.
Rosi, N. L., Eckert, J., Eddaoudi, M., Vodak, D. T., Kim, J., O'Keeffe, M. & Yaghi, O. M. (2003). *Science*, **300**, 1127–1129.
Rowsell, J. L. C., Millward, A. R., Park, K. S. & Yaghi, O. M. (2004). *J. Am. Chem. Soc.* **126**, 5666–5667.
Sakata, M. & Sato, M. (1990). *Acta Cryst.* A**46**, 263–270.
Sawa, H., Wakabayashi, H., Murata, Y., Murata, M. & Komatsu, K. (2005). *Angew. Chem. Int. Ed.* **44**, 1981–1983.
Seo, J. S., Whang, D., Lee, H., Jun, S. I., Oh, J., Jeon, Y. J. & Kim, K. (2000). *Nature (London)*, **404**, 982–986.
Shimotani, H., Ito, T., Iwasa, Y., Taninaka, A., Shinohara, H., Nishibori, E., Takata, M. & Sakata, M. (2004). *J. Am. Chem. Soc.* **126**, 364–369.
Sivia, D. S. & David, W. I. F. (1994). *Acta Cryst.* A**50**, 703–714.
Snyder, G. J., Christensen, M., Nishibori, E., Caillat, T. & Iversen, B. (2004). *Nature Materials*, **3**, 458–463.
Sugai, T., Inakuma, M., Hudgins, R., Dugourd, P., Fye, J. L., Jarrold, M. F. & Shinohara, H. (2001). *J. Am. Chem. Soc.* **123**, 6427–6428.
Takaoka, K., Kawano, M., Ozeki, T. & Fujita, M. (2006). *Chem. Commun.* pp. 1625–1627.y
Takata, M., Nishibori, E., Kato, K., Kubota, Y., Kuroiwa, Y. & Sakata, M. (2002). *Adv. X-ray Anal.* **45**, 377–384.
Takata, M., Nishibori, E., Kato, K., Sakata, M. & Moritomo, Y. (1999). *J. Phys. Soc. Jpn*, **68**, 2190–2193.
Takata, M., Nishibori, E., Sakata, M., Inakuma, M., Yamamoto, E. & Shinohara, H. (1999). *Phys. Rev. Lett.* **83**, 2214–2217.
Takata, M. & Sakata, M. (1996). *Acta Cryst.* A**52**, 287–290.
Takata, M., Umeda, B., Nishibori, E., Sakata, M., Saito, Y., Ohno, M. & Shinohara, H. (1995). *Nature (London)*, **377**, 46–49.
Tan, K. & Lu, X. (2006). *J. Phys. Chem. A*, **110**, 1171–1176.
Tanaka, H., Kuroiwa, Y. & Takata, M. (2006). *Phys. Rev. B*, **74**, 172105.
Tanaka, H., Takata, M., Nishibori, E., Kato, K., Iishi, T. & Sakata, M. (2002). *J. Appl. Cryst.* **35**, 282–286.
Vries, R. Y. de, Briels, W. J. & Feil, D. (1994). *Acta Cryst.* A**50**, 383–391.
Wang, C. R., Kai, T., Tomiyama, T., Yoshida, T., Yuji, K., Nishibori, E., Takata, M., Sakata, M. & Shinohara, H. (2001). *Angew. Chem. Int. Ed.* **40**, 397–399.
Wilkins, S. W., Varghese, J. N. & Lehmann, M. S. (1983). *Acta Cryst.* A**39**, 47–60.
Yaghi, O. M., O'Keeffe, M., Ockwig, N. W., Chae, H. K., Eddaoudi, M. & Kim, J. (2003). *Nature (London)*, **423**, 705–714.